

Drogue Motion Estimation Using Air-to-Air Observations

Daniel B. Wilson, Ali Haydar Göktoğan and Salah Sukkarieh

The Australian Centre for Field Robotics (ACFR)

The University of Sydney, Australia

[d.wilson, a.goktogan, s.sukkarieh] at acfr.usyd.edu.au

Abstract

Autonomous aerial docking for energy replenishment promises to unlock important unmanned aerial vehicle capabilities by extending range, time on target and reducing fuel usage by eliminating refueling stop-overs. The passive probe and drogue docking method has been used with manned aircraft for decades but requires accurate relative navigation for successful docking. To address this, we propose a drogue estimation framework that uses a derived system model, vehicle state information and air-to-air visual observations to estimate drogue position, motion and aerodynamic coefficients. Outdoor experiments demonstrate the infra-red vision system operating in real-time while high fidelity simulation verifies the estimation framework and display graceful degradation in accuracy when visual information is unavailable.

1 Introduction

Autonomous aerial docking for unmanned aerial vehicles (UAV) has yet to be accomplished and will be a significant milestone in UAV autonomy. One compelling application of this technology is the automated transfer of energy from one aircraft to another to eliminate the need to return to base. With biological constraints already removed, the impact of aerial energy replenishment is significant and far reaching. In the military domain, operational range and time on target is greatly increased, without sacrificing payload capacity. In a civilian context, fuel usage reductions around 30-40 percent have been suggested for international and haulage flights through the elimination of refueling stop-overs [Nangia, 2006].

UAV aerial docking is a large, complex, multi-disciplinary problem that demands reliable operation during all phases of the mission which includes rendezvous, formation flight, docking and station keeping.



Figure 1: A UAV towing a drogue.

Of these, docking is considered the most challenging phase due to the close proximity and high accuracy relative estimation and control requirements. Two manned aircraft refueling strategies that are currently employed are an actively controlled boom method which requires a human operator in the tanker aircraft and a passive probe and drogue method which defers responsibility to the following aircraft to perform docking. Of these methods, the probe and drogue strategy is considered in this work because it is more compact, it supports multiple vehicles concurrently and requires the highest relative navigation performance.

The work herein addresses drogue relative sensing and estimation, with an emphasis on accuracy, reliability and timeliness to broaden the application to small, dynamic UAVs. An unscented Kalman filter (UKF) is used to estimate the position, velocity and aerodynamic coefficients of the drogue. A derived model propagates the system using leader state information and estimate updates are provided by a monocular infra-red (IR) camera which is mounted on the follower and observes IR markers on the drogue. An efficient algorithm fits an ellipse to the observations and if successful, the ellipse parameters form pseudo sensor measurements. The ellipse fitting strategy negates the need for a marker model, avoids difficult correspondence determination and allows the drogue to rotate about its axis. Further, drogue aerodynamic coefficient estimation allows the estimate ac-

curacy to degrade gracefully when observations become unavailable. The drogue state is estimated relative to the leader to form a desired formation configuration for docking guidance, but can be calculated relative to the follower by adding the known, accurate relative position.

Outdoor experiments with an IR video stream and IR markers have demonstrated the ellipse extraction algorithm successfully operating in real-time. High fidelity simulation results show good agreement with the truth as well as graceful degradation when visual measurements are unavailable for both brief and extended periods.

1.1 Related Work

Previous work has almost exclusively focused on direct pose estimation with relative observations. [Chen and Stettner, 2011] used flash LIDAR 2D intensity to segment the drogue, then calculated the relative pose using the 3D point cloud. [Scott *et al.*, 2007] was able to post-process actual refueling footage to extract the drogue by taking advantage of the high contrast and consistent shape of the refueling hub. These measurements were then used to calculate the range with accuracy sufficient for docking of large scale aircraft. Monocular template matching, image segmentation and image registration to detect and track a drogue in [Martinez *et al.*, 2013]. High fidelity hardware-in-the-loop experiments with actual refueling hardware demonstrated the accuracy and reliability of the approach. Active deformable visual contours were used in [Doebbler *et al.*, 2006] to estimate the relative pose of a receiver for refueling boom active control.

Similarly to our work, [Mati *et al.*, 2006] uses observations to drogue mounted active markers to resolve the relative pose. Solutions to marker correspondence determination and pose estimation are provided and validated in simulation. [Valasek *et al.*, 2005] proposed an IR camera-marker system called VISNAV. A communication link orchestrates beacon activation timing to solve correspondence determination and a Gaussian least-square differential-correction algorithm resolves the relative pose from the marker measurements.

Our work differs from the feature-based methods by extracting higher-order information through an ellipse fitting procedure. This negates the need for correspondence determination, direct pose estimation and an accurate marker model, provided the approximate geometry of the drogue is known. Further, each of these direct methods rely on consistently available data and will therefore fail when the drogue is outside the FOV, heavily occluded or the algorithm itself fails. To alleviate this, we propose an indirect method within an UKF framework that estimates the orientation of the drogue cable with respect to the tanker, and propagates the system using tanker sensor measurements, known drogue

geometric characteristics and aerodynamic coefficients which are estimated online, within the filter. Pseudo measurements in the form of detected ellipse parameters update the cable orientation and refine the aerodynamic coefficients to maintain a reasonable estimate when visual measurements are unavailable.

Work on hose and drogue modelling has received a lot of attention due to the challenges associated with the flexible hose. Numerous methods of varying fidelity and complexity have been proposed, however the common approach is to approximate the bending structure with n connected linkages, each subject to gravitational and aerodynamic loads due to tanker wake, steady wind and atmospheric turbulence [Ro and W. Kamman, 2010; Vassberg *et al.*, 2003]. For tractability within the filter, we simplify this by modelling the cable as a single rigid linkage, with negligible mass and aerodynamics. This assumption has been shown to be valid in flight experiments with small UAVs, an example of which is shown in Fig. 1.

The remainder of the paper begins in Section 2 by describing the problem constraints and assumptions. Section 3 provides the process and observation models that are used within the filter and introduces the ellipse extraction algorithm. Outdoor tests and simulated results verify the ellipse extraction algorithm and drogue estimator in Section 4. Conclusions and suggestions for a future direction are provided in Section 5.

2 Problem Formulation

In our scenario, two UAVs are flying in leader-follower formation as shown in Fig 2. The leader UAV is towing a drogue with radius r , depth d and has ≥ 5 IR LED markers mounted around the edge of the circular drogue entry. Five markers are also mounted at the extremities of the leader aircraft and although they are not explicitly used in this work, they are included because they are used to estimate the vehicle-to-vehicle relative state and appear in the IR images. The drogue is modelled as a point mass, m and is attached to the leader by a rigid cable at point P_{cable} in the leader's body frame. A ball and socket joint is present at P_{cable} and P_d . The cable is of length L and has negligible mass and aerodynamics. An aerodynamic force F_D and gravitational force F_G act at P_d . The cable makes a longitudinal angle θ and lateral angle β with the horizontal plane, in the direction of the aircraft's wind frame.

A monocular IR camera mounted at the front of the follower observes the IR markers. It is assumed that a noise corrupted estimate of the relative position $P_{l|f}$ in the north-east-down navigation frame, leader attitude $[\phi_l \ \theta_l \ \psi_l]^T$, follower attitude $[\phi_f \ \theta_f \ \psi_f]^T$, leader airspeed V_a and leader vertical velocity v_z in the navigation frame, are known via wireless communication.

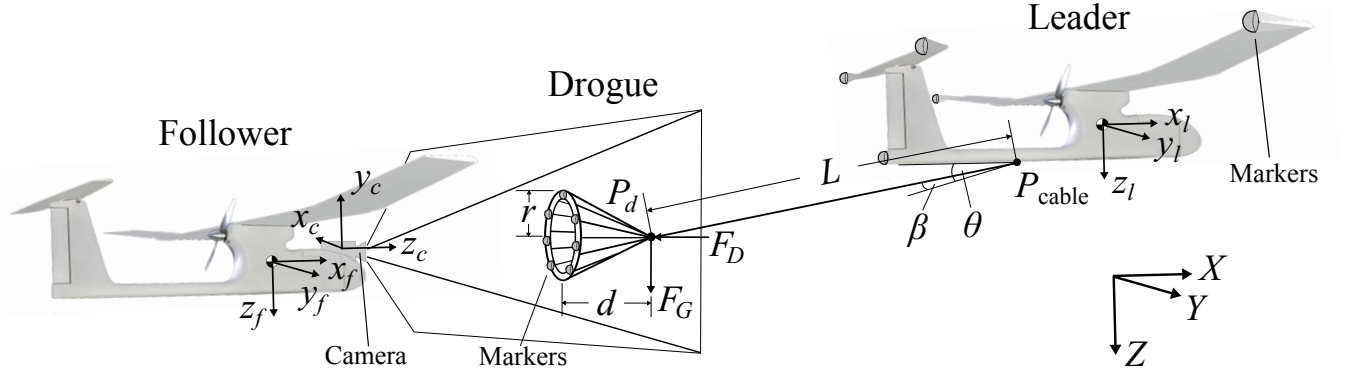


Figure 2: Coordinate frames, IR vision system and drogue geometry.

Table 1: The cable-droge geometric parameters.

Parameter	Description	Value
L	cable length	3.0 m
r	drogue radius	0.16 m
d	drogue depth	0.4 m
m	drogue mass	0.2 kg
P_{cable}	cable position	$[-0.34, 0, 0.095]$ m

Further, it is assumed the camera extrinsic and intrinsic parameters have been identified.

In our work, we consider small UAVs, operating in the turbulent lower atmosphere. Despite these difficult problem parameters, we adopt the rationale that sensors, systems and algorithms that successfully operate on these platforms can be scaled up to larger vehicles. The geometric parameters used in our work are provided in Table 1.

3 Droge Estimation

This section describes the droge state estimation framework. First, the process model that governs the droge dynamics is described. This model is driven by the leader's sensed velocity, the droge's known mass and geometric characteristics and the estimated droge aerodynamic coefficients. Then, the ellipse extraction algorithm and its corresponding observation model is described. A UKF forms the framework of the estimator.

The state vector being estimated, \mathbf{x} in Eq. (1) comprises the orientation of the cable, θ and β ; their respective time derivatives $\dot{\theta}$ and $\dot{\beta}$; and the product of the droge cross-sectional area and the aerodynamic drag coefficient for the axial direction, η_x and the lateral plane η_{yz} .

$$\mathbf{x} = [\theta \quad \dot{\theta} \quad \beta \quad \dot{\beta} \quad \eta_x \quad \eta_{yz}]^T \quad (1)$$

$$\eta_x = A_x C_{D_x} \quad (2a)$$

$$\eta_{yz} = A_{yz} C_{D_{yz}} \quad (2b)$$

The system inputs, \mathbf{u} are defined in Eq. (3) and comprise the leader airspeed V_a , leader vertical velocity v_z and the mean of the Gaussian noise processes that govern η_x and η_{yz} . The corresponding process noise covariance matrix \mathbf{Q} is defined in Eq. 4.

$$\mathbf{u} = [V_a \quad v_z \quad 0 \quad 0]^T \quad (3)$$

$$\mathbf{Q} = \text{diag} [\sigma_{V_a}^2 \quad \sigma_{v_z}^2 \quad \sigma_{\eta_x}^2 \quad \sigma_{\eta_{yz}}^2]^T \quad (4)$$

An initial estimate for \mathbf{x} is shown in Eq. (6) where θ_0 is determined in Eq. (5) by calculating the angle between F_{D_x} and F_G . β_0 and the initial orientation time derivatives are assumed to be zero. η_x and η_{yz} are initialised to 0.0096 and 0.0058 respectively as a rough guess, driven by a droge's reported drag coefficient of 0.6 [Ro *et al.*, 2011] and the geometry specified in Table 1.

$$\theta_0 = \tan^{-1} \frac{mg}{\frac{1}{2}\rho\eta_x V_a^2} \quad (5)$$

$$\mathbf{x}_0 = [\theta_0 \quad 0 \quad 0 \quad 0 \quad 0.0096 \quad 0.0058]^T \quad (6)$$

3.1 Process Model

The Cartesian coordinates of the connection between the droge and cable, P_d is calculated by rotating the cable length L through the current cable orientation estimate, θ and β as shown in Eq. (7). The velocity V_d of P_d is provided in Eq. (8).

$$P_d = C_{(0,\theta,\beta)}^T \begin{bmatrix} -L \\ 0 \\ 0 \end{bmatrix} \quad (7)$$

$$V_d = \begin{bmatrix} 0 \\ \dot{\theta} \\ \dot{\beta} \end{bmatrix} \times P \quad (8)$$

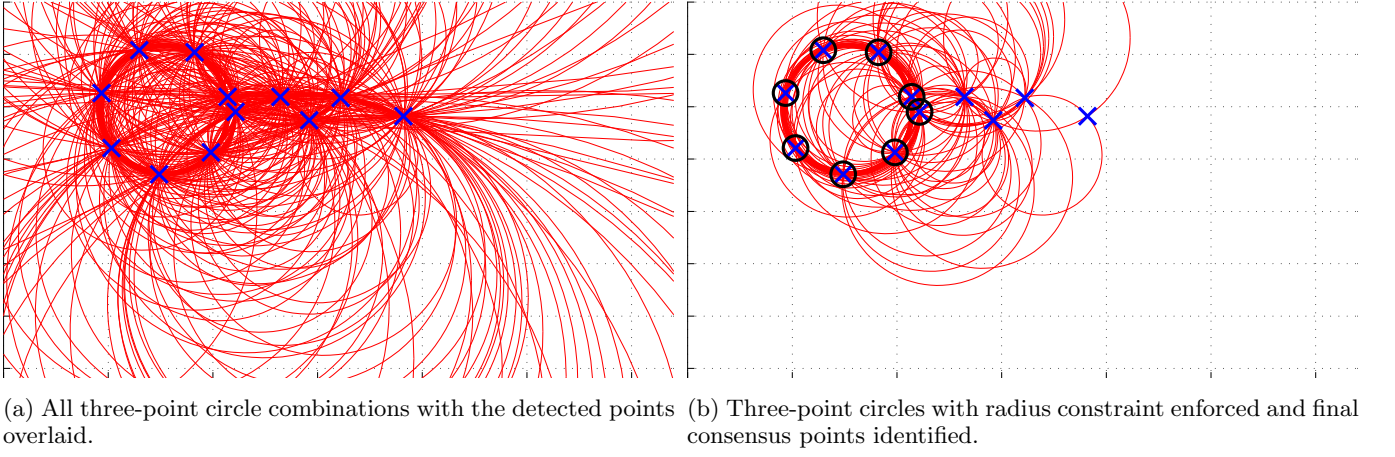


Figure 3: The ellipse extraction algorithm.

Equation (9) shows the rotation matrix notation that describes $C_{(x,y,z)}$, a rotation through the Euler angles $[x \ y \ z]^T$, where $cx = \cos x$ and $sx = \sin x$. Further, a transformation from frame x to frame y is defined as C_x^y with subscript l, f, n and c representing the leader's body frame, follower's body frame, navigation frame and camera frame, respectively.

$$C_{(x,y,z)} = \begin{bmatrix} cy\ cz & cy\ sz & -sy \\ sx\ sy\ cz - cx\ sz & sx\ sy\ sz + cx\ cz & sx\ cy \\ cx\ sy\ cz + sx\ sz & cx\ sy\ sz - sx\ cz & cx\ cy \end{bmatrix} \quad (9)$$

The air-relative velocity V_{a_d} , of P_d , in the navigation frame is calculated in Eq. (10). It is assumed that the wind acts only in the horizontal frame so that $V_{a_z} = v_z$ and that V_a is purely longitudinal so that $V_{a_y} = 0$.

$$V_{a_d} = V_{d|l} + \begin{bmatrix} V_a \\ 0 \\ v_z \end{bmatrix} \quad (10)$$

The drag force F_D and gravitational force F_G are calculated in Eq. (11) and Eq. (12) respectively. Equation (11) is negated because the drag force acts in the opposite direction to the air-relative velocity. ρ represents air density.

$$F_D = -\frac{1}{2} \rho \begin{bmatrix} \eta_x \\ \eta_{yz} \end{bmatrix} V_{a_d}^2 \frac{V_{a_d}}{\|V_{a_d}\|} \quad (11)$$

$$F_G = \begin{bmatrix} 0 \\ 0 \\ mg \end{bmatrix} \quad (12)$$

The moment M about P_{cable} is calculated in Eq. (13). The inertia tensor I is calculated in Eq. (14) before

being inverted to calculate the angular acceleration α and hence the second derivative of the cable orientation, $\ddot{\theta}$ and $\ddot{\beta}$ in Eq. (15).

$$M = P_d \times (F_D + F_G) \quad (13)$$

$$I = m \begin{bmatrix} P_y^2 + P_z^2 & -P_x P_y & -P_x P_z \\ -P_x P_y & P_x^2 + P_z^2 & -P_y P_z \\ -P_x P_z & -P_y P_z & P_x^2 + P_y^2 \end{bmatrix} \quad (14)$$

$$\alpha = \begin{bmatrix} 0 \\ \ddot{\theta} \\ \ddot{\beta} \end{bmatrix} = I^{-1} M \quad (15)$$

η_x and η_{yz} are modelled as a random walk so $\dot{\eta}_x = \dot{\eta}_{yz} = 0$. Finally, \mathbf{x} and the covariance are propagated using the UKF equations, however these and the UKF update equations have been omitted for brevity. The reader is directed to [Julier *et al.*, 1995] for more details.

$$\dot{\mathbf{x}} = [\dot{\theta} \ \ddot{\theta} \ \dot{\beta} \ \ddot{\beta} \ 0 \ 0]^T \quad (16)$$

3.2 Ellipse Extraction

Before the n raw 2D marker observations, $\tilde{\delta}_j = [u_j \ v_j]^T, j = 1, \dots, n$ can be used to correct \mathbf{x} , we must first decide which, if any $\tilde{\delta}$ belong to the drogue. The first step is to calculate all the circles from all possible three-point combinations of $\tilde{\delta}$. Each of these circle centres and radii form a hypothesis for the drogue. Three-point circles were selected because they afford a unique solution, reduce the combinatorial burden and are efficient to calculate. Figure 3a demonstrates this step with all $\tilde{\delta}$ represented by blue crosses and all hypotheses as red circles. In this particular example, $\tilde{\delta}$ is comprised of seven drogue markers and five leader aircraft mounted markers, however the number of drogue markers must

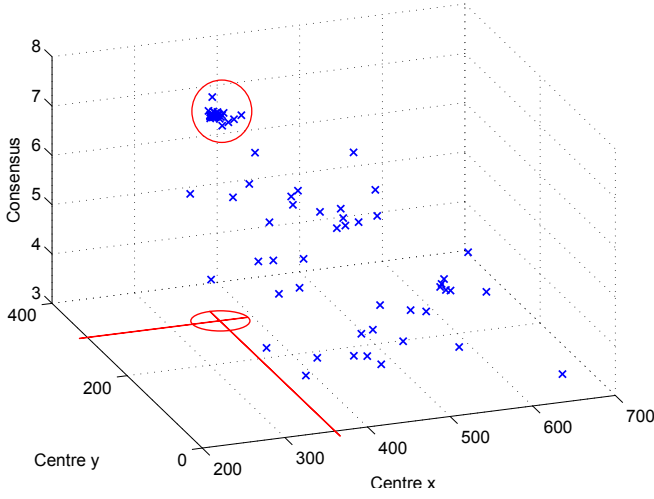


Figure 4: Strong correlation between circle centre and consensus.

only be ≥ 4 and the vehicle markers are treated as false positives.

The next step is to enforce Eq. (18) which constrains the circle radius to a range corresponding to the estimated distance of the drogue with respect to the follower $\|P_{d|f}\|$, \pm the covariance of $P_{d|f}$, $\sigma_{P_{d|f}}^2$. As both drogue estimation and vehicle relative estimation confidence improves, this bound will tighten. An example output is shown in Fig. 3b.

$$P_{d|l} = P_d + P_{cable} \quad (17a)$$

$$P_{d|f} = P_{d|l} + P_{l|f} \quad (17b)$$

$$\frac{fr}{\|P_{d|f} + \sigma_{P_{d|f}}^2\|} \geq \text{circle radius} \geq \frac{fr}{\|P_{d|f} - \sigma_{P_{d|f}}^2\|} \quad (18)$$

Next, the Euclidean distance from every $\tilde{\delta}$ to every circle hypothesis is calculated. For each hypothesis, $\tilde{\delta}$ associated with distances above a threshold are eliminated and the remaining $\tilde{\delta}$ are labelled consensus points since they provide evidence in support of the hypothesis. The total number of consensus points and the average distance error is stored for each hypothesis. Example consensus points for a given hypothesis are represented by circles in Fig. 3b.

If a circular object, consistent with a drogue is present, there will be high correlation between hypothesis centre, radius and number of consensus points and for multiple hypotheses. This is shown in Fig. 4, where a circle shows a high density of centre positions that are correlated with high consensus. The set of hypotheses with the highest consensus, over a minimum threshold, are extracted and

the hypothesis with the lowest average distance error of that set is designated most likely. Finally, an ellipse is fit to the consensus points using the direct least squares method proposed in [Fitzgibbon *et al.*, 1999] and the ellipse parameters form a higher-order pseudo measurement. The algorithm can fail at any time, which typically occurs when all hypotheses have been eliminated.

3.3 Observation Model

The observation model that corresponds to the higher-order pseudo measurement calculates the expected ellipse parameters, given the current estimate of the drogue state. First, the position in the centre of the drogue opening P_{circ} is calculated in Eq. (19) by rotating the end of the cable by θ , then adding the depth of the drogue d .

$$P_{circ} = C_{(0,\theta,0)}^T \begin{bmatrix} -L \\ 0 \\ 0 \end{bmatrix} + \begin{bmatrix} -d \\ 0 \\ 0 \end{bmatrix} \quad (19)$$

The circular drogue entry is then discretised into m evenly spaced marker positions, a distance r about P_{circ} . We use $m = 5$ to guarantee a unique ellipse. These points are then rotated by β and translated by the mounting position of the cable, P_{cable} to form the expected marker model ζ_j^l .

$$t = (j - 1) \frac{2\pi}{m} \quad (20)$$

$$\zeta_j^l = C_{(0,0,\beta)}^T \left(P_{circ} + r \begin{bmatrix} 0 \\ \sin t \\ -\cos t \end{bmatrix} \right) + P_{cable} \quad (21)$$

The expected observations $\bar{\delta}_j, j = 1, \dots, m$ are calculated by first transforming ζ_j^l from the leader's horizontal body frame to the world frame, ζ_j^f using Eq. (22). In this case the world frame is the follower's body frame.

$$\zeta_j^f = C_n^f(C_{(0,0,\psi)} \zeta_j^l + P_{l|f}) \quad (22)$$

The vision sensor extrinsic parameters transform ζ_j^f to the camera frame using Eq. (23). $P_{f|c}$ and C_f^c are the translation and rotation from the followers body frame to the camera frame. C_f^c includes both the camera mounting orientation and the axes transformation.

$$\zeta_j^c = [C_f^c \ P_{f|c}] \begin{bmatrix} \zeta_j^f \\ 1 \end{bmatrix} \quad (23)$$

$\bar{\delta}_j$ is calculated using the camera intrinsic matrix K , which encapsulates the camera focal length, aspect ratio, principal point and distortion.



Figure 6: A frame from the IR camera sequence. Each of the 12 detected markers are visible, as well as the extracted ellipse.

$$\begin{bmatrix} \bar{\delta}_j \\ 1 \end{bmatrix} = K \begin{bmatrix} \zeta_{x_j}^c / \zeta_{z_j}^c \\ \zeta_{y_j}^c / \zeta_{z_j}^c \\ 1 \end{bmatrix} \quad (24)$$

An ellipse is fit to $\bar{\delta}_j, j = 1, \dots, m$ using the method described in [Fitzgibbon *et al.*, 1999]. These elliptical geometric parameters form the pseudo-measurement observation model Eq. (25), namely the centre $\mu = [\mu_u \ \mu_v]^T$, semi major axis a , semi minor axis b and rotation φ .

$$h^{\text{vision}}(\mathbf{x}, k) = [\mu \ a \ b \ \varphi]^T \quad (25)$$

4 Experimental Results

This section provides algorithm validation and performance evaluation in two parts. The first part isolates the ellipse extraction algorithm for use as a pseudo measurement and demonstrates it working in real-time with an IR camera and IR markers, in the presence of false positives. The second part verifies the estimation algorithm using a high-fidelity multi-UAV 6DOF simulation which provides a repeatable environment where the ground truth is known. Here, realistic ground based testing is not possible because the system dynamics depend on realistic air-relative velocity.

4.1 Ellipse Extraction

The ellipse extraction algorithm was run in real-time on 20 seconds of IR camera data in an outdoor setting. Each frame was 1280×720 pixels, had a FOV of $70^\circ \times 42^\circ$ and provided 20 frames per second. The camera observed 12 markers, seven mounted on the drogue and five on a leader vehicle in a configuration representative of a pre-contact scenario, as shown in Fig. 6. The vehicle markers can be considered false positives and could be the result of ground based reflections or the sun.

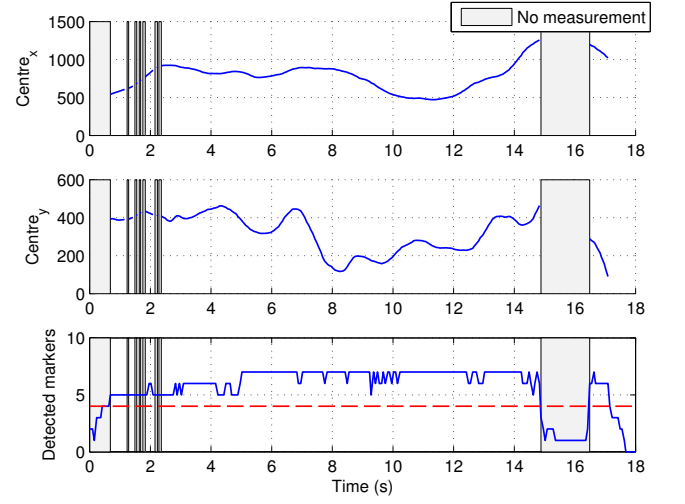


Figure 7: The centre coordinate of the extracted ellipse, when successful. The periods without a measurement typically correspond to images with less than the required five markers required for a unique ellipse and occasionally higher than allowed eccentricity at around 2 seconds.

Image processing to extract each IR point was implemented in OpenCV and was designed to maximise computational efficiency without requiring *a priori* knowledge. The marker centroids were extracted by converting the image to grayscale; thresholding; calculating image contours; approximating these with a polynomial; then returning the centre of the minimum enclosing rectangles.

Figure 7 shows the centre coordinate of the extracted ellipse and the number of detected drogue markers. The gray segments represent times when extraction was unsuccessful which can be attributed to the number of detected markers being less than the five required for a unique ellipse, which is represented by the red dashed line. At around two seconds, the extraction fails due to higher than allowed ellipse eccentricity.

4.2 Estimator Simulation

Each UAV utilises 6DOF nonlinear fixed wing equations of motion to propagate the state at 100Hz, given the control surface deflections and external disturbances. The sensors are modelled using environmental and atmospheric models with white Gaussian noise, bias and cross coupling. The GPS model also incorporates Gauss-Markov noise correlation and transport delay. The actuators are modelled with first-order time lag, saturation limits and rate saturation limits. Individual UAV state estimation is handled by a 18-state quaternion UKF; a guidance module implements a nonlinear path following strategy to follow a sequence of arcs; and cascaded,

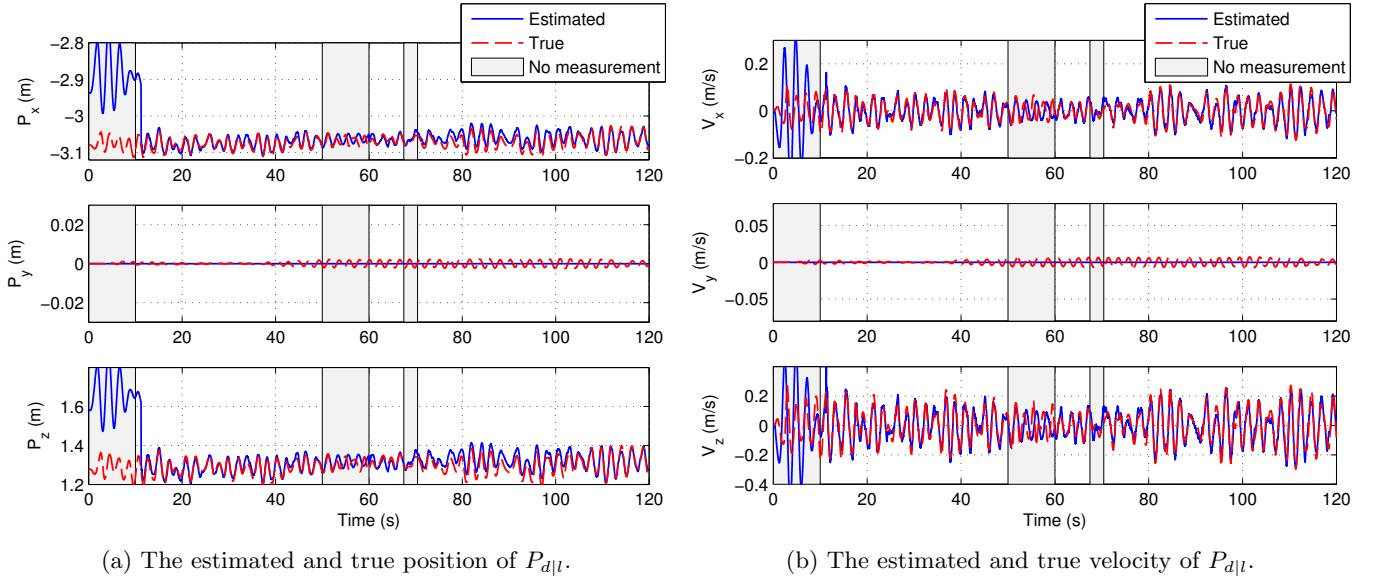


Figure 5: Drogue estimation results from a simulated leader-follower formation flight.

physics based PID controllers handle the low level actuation. The guidance, navigation and control module operates at 100Hz and is configured to automatically generate C code, in preparation for implementation in-flight. Additional details of this algorithm prototype and deployment work flow can be found in [Wilson *et al.*, 2012].

The cable was modelled as a single rigid member and the drogue as a point mass using the equations in Section 3.1. Truth values for the leader's air relative velocity were used as well as random perturbations in the lateral direction. The aerodynamic coefficients were corrupted with time varying random noise to add stochasticity to the motion.

The vision sensor was modelled with a resolution of 1280×720 pixels and a FOV of $70^\circ \times 42^\circ$ at 20 frames per second to match the hardware used in Section 4.1. The true pixel coordinates were calculated using the true vehicle states and Equations (22) to (24). The simulated measurements were created by adding white noise and placing the points in a random order. Points outside the FOV were set to zero.

The simulated scenario consisted of a leader following a 700×500 m racetrack pattern with rounded corners of radius 100m. The aircraft had a commanded altitude of 80m and commanded airspeed of 25m/s. A follower UAV was commanded to maintain equivalent airspeed and altitude to the leader at a position 7m directly behind, and 1m below the leader. This was achieved using the vision-aided relative estimation framework described in [Wilson *et al.*, 2014] and an augmented state based formation guidance algorithm that acts explicitly on the

estimated relative state. To demonstrate the estimators resilience to measurement dropouts, artificial dropouts were simulated at 0-10s and 50-60s. Measurements were also unavailable at 67-70s when the drogue was outside the FOV.

The estimated position and velocity of $P_{d|l}$ from a 120s segment of simulated flight is shown in Figures 5a and 5b. Here, we see good agreement between the true and estimated values, once measurements have been received. The accuracy of the open loop estimate during the first 10s is a function of the accuracy of the initial guess for η_x and η_{yz} . Once measurements are available, η_x quickly converges to the true value, even with 30% initial error. Estimating this parameter allows graceful degradation in accuracy during subsequent measurement outages during 50-60s and 67-70s. Without estimating this parameter or having accurate knowledge *a priori*, accuracy would quickly degrade to that of 0-10s during the subsequent outages. The estimate of η_{yz} shows a much slower convergence due to the lack of excitation in these axes. This also means that the accuracy of η_{yz} does not weigh heavily on the accuracy of $P_{d|l}$.

5 Conclusion

Autonomous UAV docking is a very difficult, but immensely powerful capability that promises to change the way we conduct UAV operations. The work presented here has addressed the problem of drogue motion estimation during the critically important pre-contact phase. In addition to the position and motion of the drogue, our approach estimates important aerodynamic coefficients

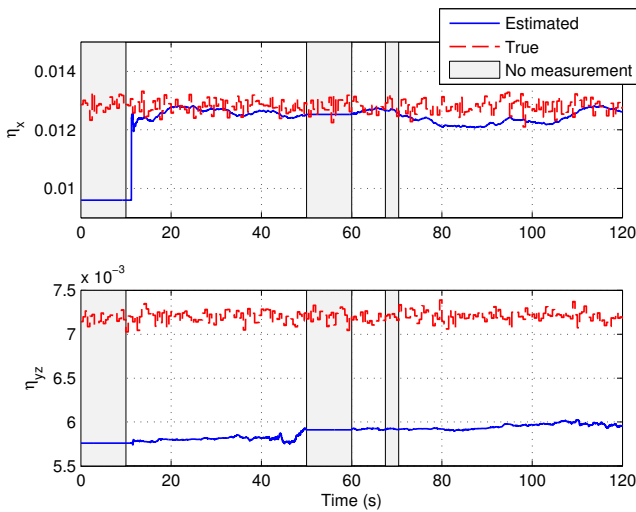


Figure 8: The estimated and true value of the product of cross sectional area and drag coefficient in the x-axis and yz-axis.

which allows the estimate accuracy to only slowly degrade when measurement updates are unavailable. This is in contrast to almost all the previous work which relies exclusively on often unreliable relative observations. Further, by extracting higher-order information in the form of an ellipse, we avoid the difficult correspondence determination problem, pose estimation problem and negate the need for an accurate marker model. Future work aims to demonstrate this algorithm operating in a close formation airborne experiment.

Acknowledgments

This work is supported by the Australian Centre for Field Robotics (ACFR) at The University of Sydney.

References

- [Chen and Stettner, 2011] C. Chen and R. Stettner. Drogue tracking using 3D flash lidar for autonomous aerial refueling. In *Proc. SPIE 8037, Laser Radar Technology and Applications XVI*, volume 8037, June 2011.
- [Doebbler et al., 2006] J. Doebbler, J. Valasek, M. J. Monda, and Hanspeter S. Boom and Receptacle Autonomous Air Refueling Using a Visual Pressure Snake Optical Sensor. In *AIAA Atmospheric Flight Mechanics Conference and Exhibit*. American Institute of Aeronautics and Astronautics, 2006.
- [Fitzgibbon et al., 1999] A. W. Fitzgibbon, M. Pilu, and R. B. Fisher. Direct least-squares fitting of ellipses. *IEEE Transactions on Pattern Analysis and Machine Intelligence*, 21(5):476–480, May 1999.
- [Julier et al., 1995] S. J. Julier, J. K. Uhlmann, and H. F. Durrant-Whyte. A new approach for filtering nonlinear systems. In *American Control Conference, Proceedings of the*, 1995.
- [Martinez et al., 2013] C. Martinez, T. Richardson, P. Thomas, L. B. Jonathan, and P. Campoy. A vision-based strategy for autonomous aerial refueling tasks. *Robotics and Autonomous Systems*, 61(8):876–895, 2013.
- [Mati et al., 2006] R. Mati, L. Pollini, A. Lunghi, M. Innocenti, and G. Campa. Vision-based autonomous probe and drogue aerial refueling. In *Control and Automation, MED’06. 14th Mediterranean Conference on*, 2006.
- [Nangia, 2006] R. K. Nangia. Operations and aircraft design towards greener civil aviation using air-to-air refuelling. *The Aeronautical Journal*, 110(1113):705–721, November 2006.
- [Ro and W. Kamman, 2010] K. Ro and J. W. W. Kamman. Modeling and simulation of hose-paradrogue aerial refueling systems. *Journal of Guidance, Control, and Dynamics*, 33(1):53–63, 2010.
- [Ro et al., 2011] K. Ro, T. Kuk, and J. W. Kamman. Design, Test and Evaluation of an Actively Stabilized Drogue Refueling System. In *Infotech@Aerospace Conferences*. The American Institute of Aeronautics and Astronautics, 2011.
- [Scott et al., 2007] D. Scott, M. Toal, and J. Dale. Vision-based sensing for autonomous in-flight refueling. In *Unmanned Systems Technology IX*, volume 6561, May 2007.
- [Valasek et al., 2005] J. Valasek, K. Gunnam, J. Kimmet, J. L. Junkins, D. Hughes, and M. D. Tandale. Vision-based sensor and navigation system for autonomous air refueling. *Journal of Guidance, Control, and Dynamics*, 28(5):979–989, 2005.
- [Vassberg et al., 2003] J. C. Vassberg, D. T. Yeh, A. J. Blair, and J. M. Evert. Numerical simulations of KC-10 wing-mount aerial refueling hose-drogue dynamics with a reel take-up system. In *21st Applied Aerodynamics Conference*, 2003.
- [Wilson et al., 2012] D. B. Wilson, A. H. Göktoğan, and S. Sukkarieh. UAV Rendezvous: From Concept to Flight Test. In *Australasian Conference on Robotics and Automation (ACRA)*, 2012.
- [Wilson et al., 2014] D. B. Wilson, A. H. Göktoğan, and S. Sukkarieh. A Vision Based Relative Navigation Framework for Formation Flight. In *Robotics and Automation (ICRA), 2013 IEEE International Conference on*, 2014.